August 1992
To be published in The Microbeam Analysis Journal

BNL--48003

DE93 001975

SYNCHROTRON RADIATION INDUCED X-RAY MICRO ANALYSIS: A REALISTIC ALTERNATIVE FOR ELECTRON- AND ION BEAM MICROSCOPY?

K. Janssens and F. Adams

Department of Chemistry, University of Antwerp (U.I.A.), Wilrijk/Antwerp, Belgium

M. L. Rivers and K. W. Jones

Department of Applied Science, Brookhaven National Laboratory, Upton, New York 11973

Presented at

1992 Microbeam Analysis Society Meeting

Boston, Massachusetts

August 16-21, 1992

SYNCHROTRON RADIATION INDUCED X-RAY MICRO ANALYSIS: A REALISTIC ALTERNATIVE FOR ELECTRON- AND IONBEAM MICROSCOPY ?

K. Janssens[1], F. Adams[1], M.L. Rivers[2], K.W. Jones[2],
[1]Department of Chemistry, University of Antwerp (U.I.A.)
Universiteitsplein 1, B-2610 Wilrijk/Antwerp, Belgium
[2]Department of Applied Science, Brookhaven National Laboratory,
Upton, Long Island, New York 11973, USA

Short title: Synchrotron Radiation Induced X-ray Micro Analysis.

Send correspondence to:

Dr. Koen Janssens
Department of Chemistry
University of Antwerp (U.I.A.),
B-2610 Antwerp/Wilrijk, Belgium
EUROPE
Tel.: +32 3 828.23.73 Fax: +32 3 828.23.76

Abstract

Synchrotron Radiation induced X-ray micro Fluorescence analysis (μ-SRXRF) is compared with more conventional microanalytical techniques such as Secondary Ion Microscopy (SIMS) and Electron Probe X-ray Microanalysis (EPXMA) for two typical microanalytical applications. SRXRF and EPXMA are employed for the analysis of individual particles, showing the complementary character of both techniques. By means of element mapping of trace constituents in a heterogeneous feldspar, the strong and weak points of SRXRF in comparison to EPXMA and SIMS are illustrated. The most striking difference between SRXRF and the other two microanalytical methods is the ability of SRXRF to probe deep into the investigated material, whereas SIMS and EPXMA only investigate the upper surface of the material. The possibilities of SRXRF at third generation synchrotron rings is also briefly discussed.

1. Introduction

During the last decade, a number of microanalytical methods have come into existence which are capable of yielding information on the lateral distribution of elemental species in solid materials. A number of these methods and some of their properties are listed in Table I. A few of these techniques are the microscopic analoges of bulk analytical methods which have been in use for a much longer time and have opened new horizons in an already established field. Such is the case for synchrotron radiation induced X-ray fluorescence (SRXRF). Conventional (tube-excited) XRF analysis, either in its energy-dispersive (ED) or wavelength dispersive (WD) form, is a widespread analytical method which allows for reliable multielement analysis of bulk specimen at the ppm level.

The use of synchrotron radiation for XRF work was initiated by Sparks (Sparks et al., 1980). In the last 5 years, as a result of the increasing availability of electron storage rings as sources of highly intense, collimated and polarized X-rays in the energy range between 1 and 30-40 keV, around the world, a number of X-ray fluorescence microprobes have been constructed. At Hasylab (Hamburg, FRG) and at the NSLS (Brookhaven National Laboratories, Upton, NY, USA), white light microprobes are in operation (Bavdas et al. 1988; Jones and Gordon, 1989). Using collimated pencil beams, sensitive trace element mapping with minimum detection limits in the 1-10 ppm range can be performed with a lateral

resolution of the order of 10 µm. At SRS (Daresbury, UK), at SSRL (Stanford, CA, USA) and at the Photon Factory (Tsukuba, Japan), focussed monochromatic microbeams are employed (Van Langevelde et al., 1990; Thompson et al., 1988; Goshi et al., 1987).

As can be seen from Table I, SRXRF represents a unique combination of qualities which cannot be found in any of the other microanalytical methods listed. As with secondary ion microscopy (SIMS), SRXRF is capable of trace level microanalysis but does have any of the disadvantages associated with a destructive mass spectrometric technique such as SIMS or LAMMA (Laser Mass Micro Analysis). Combining sensitive elemental mapping with the proven accuracy and reliability of quantitative XRF makes SRXRF a very interesting analysis technique. Since SIMS and SRXRF are based on very different microbeam-matter interactions, making an objective comparison on other than the overall performance of the methods is difficult.

A more detailed comparison can be made when SRXRF is considered next to its closest analogues: µ-PIXE (Particle Induced X-ray Emission) and EPXMA (Electron probe X-ray microanalysis). Essentially, these three methods only differ in the type of energy carriers that are being used in the microbeam; all are based on the creation of inner shell vacancies in target atoms and rely on the detection of the resulting element specific radiation using energy-dispersive Si(Li) detectors. The strong and weak points of

SRXRF can be seen from a consideration of the production cross sections for photon, electron and proton induced X-radiation emission as a function of atomic number and particle energy. Fig. 1 shows that at excitation energies below 20 keV, photon induced X-ray emission is about a factor of 10 to 100 more efficient that electron- or proton based excitation. This means that per characteristic X-ray produced, the energy deposition in the sample using SRXRF is also a factor 10-100 lower than in the case of EPXMA; this difference is even larger in the case of μ-PIXE (Mazzolini et al., 1981; Vis, 1988). A second important difference between photon vs. electron or proton induced X-ray production is the dependence of the production cross sections on the target atomic number Z. As can be seen in Fig. 1, in the case of charged particles, the cross sections decrease with rising Z whereas they increase in the case of photon excitation. As a result, EPXMA and to a lesser extent μ-PIXE are very suitable for the determination of low-Z elements whereas SR-XRF is more appropriate for visualising distributions of species of higher atomic number. In a comparison between μ-PIXE and SRXRF, for the analysis of biological specimen, Van Langevelde et al. (1990) concluded that for Z > 20 (Ca), the monoenergetic (15 keV) X-ray microprobe at SRS provides better MDL (minimum detection limit) values than a proton microprobe.

Another important difference between the interaction of photons and charged particles with matter is the probability for scatter interactions. As a result of many (in)elastic encounters, the

retardation of energetic charged particles into solids gives rise to a bremsstrahlung continuum in the detected X-ray spectra. In the case of X-ray fluorescence, each primary photon only undergoes one or two scattering interactions within the sample atoms it is either absorbed (photo-ionisation) or escapes from the solid. This results in nearly background-free XRF spectra in case monochromatic photon excitation is employed, yielding (sub)ppm level detection limits for selected elements (Van Langevelde et al., 1990). Only in the region at and just below the primary energy, (in)coherent scatter peaks significantly contribute to the background. The linear polarisation of synchrotron radiation in the plane of the storage ring further decreases the background level when the Si(Li) detector is also positioned in this plane at 90° to the incident beam. This effect makes it possible to achieve ppm level MDL values with SRXRF employing polychromatic excitation (Jones and Gordon, 1989).

SRXRF also has the additional major benefit that, in contrast to charged particle techniques, sample materials need not be placed in vacuum and need not be conducting; the penetrating nature of the X-rays facilitates the use of wet cells and similar devices for *in vivo* type of measurements.

In the past, a number of papers have been published in which the qualities of SRXRF are compared for bulk analysis with PIXE (Bos et al., 1984; van Langevelde et al., 1990), with tube-excited XRF (Jones et al., 1984, Bos et al., 1984) and with radio-isotope

excited EDXRF (Baryshev et al., 1987; Török et al., 1989). In a previous paper, (Janssens et al., 1992), we have compared the use of a monochromatic and a polychromatic X-ray microprobe to that of an electron- and proton microprobe for individual particle analysis. This study, which involved the analysis of standard NIST glass microspheres, revealed large differences in the analytical qualities of the two X-ray microprobes. In terms of speed of analysis and achievable detection limits, the white light X-ray microprobe at NSLS and the electron microprobe proved to be the most appropriate for characterisation of large numbers of individual particles. Using the white light X-ray microprobe, MDL values for, e.g., Ca and Fe were found to be resp. 10 and 2 ppm in 20 μm particles for a 100 sec counting interval. This study also revealed that the NSLS X-ray microprobe is limited to analysing particles with diameters larger than ca. 5 μm.

As a continuation of these investigations, the first part of present work discusses the analysis of a 'real' particle set using EPXMA and white beam SRXRF. Individual aerosol particles collected on the Antarctic during the summer and winter of 1988 were analysed in order to assess the composition and relative importance of the various aerosol sources in this remote area. Antarctica is supposed to suffer minimally from anthropogenic pollution, although the concentrations of several trace gases are known to be increasing over this continent. The recent interest in the Antarctic atmosphere has resulted in a recognition of the need for detailed

aerosol characterization studies. The (dis)advantages of the two analytical methods in terms of speed of analysis, sensitivity and their ability to classify particles into various classes is discussed.

Next to the analysis of minute samples such as micrometeorites, aerosols and water-suspended particulate matter, SR-XRF can also be employed for visualising the distribution of elemental species in larger samples. This type of measurement involves the scanning of the microbeam over a selected area of the sample surface while signals originating from each location are collected and sorted accordingly. Published reports mainly deal with investigations in the biological and geological field (see, e.g., Frantz et al., 1988; Kwiatek et al., 1987; Jones et al., 1992). Usually, thin sections of minerals, resp. tissues are studied and lateral resolutions approx. equal to the dimensions of the photon beam are achieved. From a general analytical point of view, however, it is also of interest to compare the performance of SRXRF when non-thin samples are studied; a large number of industrially interesting materials such as ceramics are either too brittle or too sensitive to allow elaborate sample preparation procedures to be used; the latter can also be a source of contamination (see below).
In the second part of this work, SRXRF is compared with SIMS and EPXMA for elemental mapping of major and trace constituents in a thick sample of a feldspar mineral. This material was studied because of its microhetergeneity both at the major and and trace

levels. Attention is devoted to the lateral resolution attainable in the elemental maps and the factors that influence it and to the sensitivity of the various techniques.

Finally, the predicted analytical qualities of an SRXRF station which may be installed in the next few years at a beam line of a third generation X-ray source such as the European Synchrotron Radiation Facility (ESRF), now under construction in Grenoble, France will be briefly discussed.

2. Materials and Methods

The antarctican aerosols were first collected during the summer and winter of 1988 at the Brazilian Antactic station "Comandante Ferraz", on the Admiral Bay, Antarctic Peninsula. The sampling site is located 1 km from the main station and is 300 m from the sea. Details of the sampling procedure can be found in Artaxo et al. (1990). Coarse particles (with diameter > 2 μm) were collected on Nuclepore 8.0 um pore size filters. An electron micrograph of a few NaCl microcrystals found on these filters is shown in Fig. 2.

The particles were sized and analysed using a Jeol JXA-733 Electron Probe X-ray Microanalyser (Jeol Ltd., Tokyo, Japan) equipped with a Tracor Northern TN200 computer and energy-dispersive detection system. All samples were excited with an electron beam current and voltage of 1 nA and 25 kV resp. An automated particle sizing and analysis program was used to localise and collect X-ray data from about 500 particles per sample (Raeymaekers et al, 1986). In this routine, the electron beam is scanned over a selected area of the filter. A particle is detected when the backscattered electron signal exceeds a chosen threshold. For each particle, the coordinates of the particle's perimeter are determined, yielding its mean diameter. Then, the electron beam is positioned at the geometric center of the particle and an energy-dispersive X-ray spectrum is collected for each particle. In view of the large

amounts of raw data which may be collected in this way, the spectra are evaluated on-line in a semi-quantitative way; relative abundances of the elements present in the particles can be calculated from the peak areas. Per particle, the program takes about 40 sec. to perform all the above mentioned manipulations; usually analyses of this type are run overnight. Within the 500 analysed particles, approx. 100 were found to have a diameter > 5 µm. Only the latter data were used in this work. In order to reveal the various classes the particles fall into, the resulting data matrix (particle number vs. X-ray intensities of all elements found in each particle) are subjected to hierarchical cluster analsis using Ward's error sum strategy (Van Espen, 1984); in view of the limited accuracy of the on-line spectrum evaluation step, the clustering is executed in normalised X-ray intensity space rather than in concentration space (Bernard et al., 1986; Janssens et al., 1988).

For the X-ray microprobe experiments, the instrument at the X26A beamline of the NSLS (National Synchrotron Light Source) was employed. After emerging from the storage ring UHV (Ultra High Vacuum), the beam is defined by four Ta slits and further collimated by a 5x5 or 8x8 µm2 crossed slit system. The sample is positioned at 45 degrees to the incoming beam. The polychromatic energy spectrum impinging on the sample has a maximum of about 10^4 photons/sec/eV/mA/μm^2 near 8 keV. Soft X-rays (E < 4 keV) are heavily absorbed by the Be-end windows of the beam pipe and the air

path between the collimator slits and the sample. The specimen is viewed by a horizontally mounted stereozoom binocular microscope, equipped with a TV camera. For the analysis of individual particles, a 8x8 μm2 collimator was employed to define the beam size. X-ray spectra were collected by locating a particle on the filter using the microscope, moving it into the beam and maximizing the detectable countrate. This process takes about 1 to 2 min/particle. Per particle, spectrum collection times between 100 and 900 sec were employed. In contrast to the EPMA instrument, all above mentioned manipulations were executed manually, making the measurements a very time-intensive undertaking. About 3 h of instrument time were devoted to each filter; in this period, ca. 30 particles could be analysed on each sample. The X-ray data obtained from each particle were processed in the same way as was done for the EPXMA data. Clustering of the particles in normalised X-ray intensity space also proved to yield a better group separation than in concentration space. Correlations between the trace-element constituents within the various groups is studied by means of principal component analysis.

For the elemental mapping experiments, a specific 100x100 μm^2 area of a grain of Carnmenellis Granite was studied. This material consists of Na (albite) and K rich feldspar phases. The overall major and trace composition of the two minerals (Goossens et al., 1989) is listed in Table II. Details on the origin of the material can also be found in this re-reference.

The grain was imbedded in orthodontic resin, cut, and the resulting surface polished to 1 μm using diamond pastes. The surface was then gold-coated for SIMS analysis. By rastering the 30 kV O^- beam over a 250x250 μm^2 area and locally removing the gold coating by ion sputtering, a rectangular area of the underlying mineral was exposed, showing a large (30x100 μm2) albite exsolution lamella in a ground mass of K-feldspar, as shown in Fig. 3.

In this area, elemental maps were collected, first by EPXMA, then by SRXRF and finally by SIMS. During the SRXRF experiment, a collimator yielding a 5x5 μm^2 photon beam was employed. The collection of the 512x512 SIMS maps took about 2h of instrument time, including the alignment of the ion-optical system. The collection of the K and Na X-ray maps (140x200 pixels) using EPXMA took about 1h. The synchrotron radiation induced X-ray images were collected using a dwell time of 50 sec per pixel; X-ray images of 25x35 pixels in size were collected taking a total instrument time of about 12 h to acquire.

3. Individual Particle Analysis.

The results of the cluster analysis of the electron- and photon induced X-ray data derived from the Antarctican aerosol samples are summarized in Table III. The discrepancy between the abundance of the various classes can be attributed to the fact that only a limited number of particles could be analysed with SRXRF (60 particles in total) within the available beamtime. The most important fraction of the particles consists of sea-salt aerosol (see Fig. 2), showing the characteristic cubical morphology of halite microcrystals. This is similar to the results obtained by Artaxo et al. (1990) for samples collected in the same location during 1985-1987. Other classes found are soil dust and sulphate particles. In both the EPMA and the SRXRF data, the seasonal differences between summer and winter aerosols are evident. The summer data show unreacted NaCl microcrystals, freshly formed as the result of bubble bursting. In the winter sample, the Cl-rich particles also contain appreciable amounts of S and Ca and are the result of secondary reactions between marine aerosols and trace gases. EPXMA and SRXRF spectra of a particle belonging to the NaCl class (summer sample) are shown in Fig. 4 and clearly illustrate the complementarity of the two methods. Whereas in the electron-induced spectrum (Fig. 4a), only the major elements (Na and Cl) are visible, in the SRXRF spectrum, also information on minor and trace constituents such as Ca, Ti, Cr, Fe, Cu, Zn, Br, Rb and Pb is

available. E.g., the Pb signal in Fig. 4b corresponds to a concentration of about 25 ppm. The MDL value for Pb is approx. 5 ppm in this case. On the other hand, the sensitivity of the SRXRF instrument for low-Z elements (e.g., Na, Mg, Al, Si) is very low compared to that of EPXMA, making it hard even to identify the major elements of the soil dust class of aerosols, as shown in Fig. 5. This low sensivity is the result of both the small production cross section for and the considerable absorption of soft fluorescent X-rays such as Na-Kα and Mg-Kα in the SRXRF spectrometer. Despite the fact that EPXMA and SRXRF feature almost complementary sensitivity vs. atomic number characteristics, it is remarkable that very similar cluster diagrams are obtained. As an example, in Fig. 6, the dendrograms derived from the EPXMA and SRXRF data for the winter sample are shown. In both cases, three major groups of particles are readily discernable; in the EPXMA case, however, the Na and Mg signals serve to split up the Cl-rich group into subclasses. A detailed examination of the SRXRF data on the Cl-rich group in the summer data show 2 subgroups featuring resp. an average S content of 0.43±0.02 and 0.53±0.05 %w. As also reported by Artaxo et al. (1990), a large variability is found in the concentration of the trace elements within each particle group. As an illustration, Table IV lists the concentrations of a few trace elements in a number of the particles belonging one of the above mentioned Cl-rich subgroups; the particles have a diameter in the 12-15 μm, all showed the same cubical morphology and had a nearly identical major and minor composition (see sulphur data in

Table IV). The concentrations in Table IV were calculated assuming a NaCl matrix; the thicknesses of the NaCl microcrystals were estimated from the dimensions of the top face of the particles. Fig. 7 shows the result of performing principle component analysis on the complete NaCl group of particles in the summer sample. The loadings of the major and trace constituents are plotted in the space of the first two principal components. A strong correlation between K, Ca and Sr is found; this correlation is also found in the winter samples and by other workers (P. Artaxo, personal communication) and is as yet unexplained. Other correlated elements are Cr, Ni, Cu, Zn and Pb. This correlatinon may be indicative of the presence of an anthropogenic aerosol source.

4. Trace Element Imaging

In Figs. 8, 9 and 10, elemental maps are shown of various elements in the perthite material collected using respectively electron, ion and X-ray microscopy. Fig. 9 illustrates the applicability of SIMS for mapping the distribution of most elements in the periodic table; the Na and K distribution are found to be complementary, while most of the minor and trace constituents (except Ca) are concentrated in the K-rich phase. In the Al and Si maps none of the structure obtained in the other images is found.

A similar pattern in found in the EPXMA images (Fig. 8), although only maps of the major elements could be collected. Using SRXRF, again a wide range of trace constituents can be mapped; however, no data on low-Z elements below K could be obtained under the experimental conditions employed. Similar to the electron and photon induced X-ray spectra of the aerosol particles discussed above (see Figs. 4 and 5), large difference can be observed between the X-ray spectra derived from the Na and K rich phases using EPXMA and SR-XRF. As can be seen in Fig. 11a and c, only the major constituents of the minerals (Al, Si, K, Na) are visible in the electron induced spectra. In contrast, the SR-XRF spectra (Fig. 11b and d) collected at approx. the same locations on the sample show an abundance of characteristic peaks. A number of these originate from the gold coating used during the sample preparation (Au, Pt). Others, however (e.g., Mn, Fe, Pb, Sr, Rb) correspond to the trace

and minor constituents of the perthite mineral. However, the relative abundance of, e.g., Rb among the two phases is clearly not in agreement with the concentration data for this element listed in Table II. The reason for this discrepancy become clear when the elemental maps of K and Rb are considered as collected with SIMS and SR-XRF (Figs. 9 and 10 resp.). Whereas in the SIMS images irrespective of the element/mass being considered, all images show the same two-phase distribution, in the SR-XRF images, this is true only for the K, and to a lesser extent for the Ca and Ti images. In contrast, the Mn, Fe, Sr, Rb etc. maps show totally different distributions of these elements. The reason for this is the large difference in penetration depth for photon vs. electrons and heavy ions. Whereas in SIMS only the top 10-100 nm of the material is being sampled (depending on the sputter time and beam intensity), an electron beam of 25 kV will penetrate approx. 3-5 μm into the material and characteristic X-rays will emerge from a pear-shaped interaction volume of comparable size. For high energy photons, however, the penetration depth is much larger. For example, the 1/e extinction length of photons of energy 5, 10 and 20 keV in the K-feldspar phase is resp. 18, 126 and 952 μm. Accordingly, by means of the white synchrotron spectrum (which extends beyond 40 keV), a layer of material of the order of 1 to 2 mm is excited. Whereas K-Kα radiation (3.312 keV) can only escape from the topmost 10 μm thick layer, the much more energetic Rb-Kα characteristic photons (13.375 keV) have still a probability of 37 % of reaching the detector when they originate from a depth of 300 μm. In this way,

instead of only visualising the two-phase structure on the upper surface of the grain, the high energy SRXRF elemental maps yield information on structures situated deeper into the material.

In a number of application areas of synchrotron radiation, the high penetration power of energetic photons is used advantageously. E.g., by means of computed microtomography (CMT) and radiation of 60 keV obtained from a 5T super-conducting wiggler, Jones et al. (1992) were able to visualise the internal structure and density differences in a rat femur, in which an orthopedic implant (a 1 mm stainless steel pin) was cemented, yielding information on the implant-bone interface in a non-destructive way. Frantz et al. used SRXRF for probing fluid inclusions in quartz (1988) and could determine trace elements inside inclusions buried 20 to 100 µm below the surface.

On the other hand, the penetrative character of the radiation can also cause problems regarding the quantification of elemental SRXRF maps. A simple example illustrates this. At 15-20 µm diameter Fe-rich inclusion is visible at the center of the Fe-Kα map of Fig. 10. A similar structure, though less clear is discernable in the Ti, Mn and Rb images. The inclusion is located below the surface of the mineral, as it is not visible in the SIMS maps of the same region. If for simplicity, the characteristic Fe radiation is assumed to be mainly induced by radiation of average energy E_0 = 10 keV and to originate from a particular (equivalent) depth d, the Fe concentration c_{Fe} in the inclusion is related to the detected Fe-Kα intensity I_{Fe} according to:

$$I_{Fe} = G\ Q_{Fe}\ c_{Fe}\ A_{Fe}\ I(E_0)\ t = S_{Fe}\ c_{Fe}\ A_{Fe}\ t \qquad (1)$$

were G is an instrument specific constant (the geometry factor), Q_{Fe} is the production cross section for Fe-Kα radiation, A_{Fe} is an absorption factor and t is the measuring time. $I(E_0)$ is the intensity of the primary beam. S_{Fe} is called the sensitivity factor for Fe and was experimentally determined using a NIST SRM 1833 thin glass film standard. As, under the above assumptions, the absorption factor A_{Fe} is dependent on the depth of the inclusion beneath the surface d:

$$A_{Fe} = \exp\{-\rho\ d\ 1.42\ [\mu(E_0) + \mu(E)]\} \qquad (2)$$

it is clear that d must be known in order to convert the Fe-Kα intensity map of Fig. 11 into a concentration image. As the information cannot be derived from the X-ray data themselves, this presents a fundamental limitation to quantitative SR-XRF analysis of heterogeneous samples. The extent of the error that is made if an incorrent value of d is employed can be estimated from Table V, where the influence of employing various values of d chosen between 0 µm and 40 µm (the 1/e extinction depth for Fe-Kα radiation) on the maximum Fe concentration in the inclusion are listed. The calculations were done assuming the inclusion to be buried in the albite phase.

The penetration of photons into the solid also has an influence on the lateral resolution in the acquired images. In Fig. 13 cross

sections of the ^{39}K ion and K-Kα X-ray maps are plotted along a line perpendicular to the long axis of the exsolution lamella (see black line in Fig. 3). Employing a 10-90% criterion, from this plot, the width of the interface between the two phases derived from the SIMS, EPXMA and SRXRF data is estimated to be resp. 3., 5. and 12 µm. Taking diffusion of K into the albite phase into account and the lateral resolution of the SIMS instrument (< 1 µm), the first number can be considered as a reliable estimate of the true interface width. The interface width derived from the EPXMA and SRXRF data are larger as a result of the extended interaction volumina of resp. the electron and photon beam. The 5 µm interface width found in the EPXMA case is in accordance with the expected size of the interaction volume for a 25 kV electron beam (about 3.5 µm) in this case. In constrast, in the SRXRF case, although a beam of 5 x 5 μm^2 dimensions was used (measured by scanning over the edge of a thin gold edge deposited onto kapton foil), an interface width larger by a factor 2 to 3 is obtained.

This broadening cannot be explain by the scatter 'halo' of the beam. An explanation which is in accordance with the image data of Figs. 9 and 10 is schematically shown in Fig. 13b. If the albite exsolution lamella in the center of the image is assumed to have a thickness of the order of 10 to 15 µm, before the primary beam reaches the edge of the lamella (position 2) on the mineral surface, energetic photons will pass through the side of the albite layer and excite the K-rich phase. As a result, a gradual increase of the K-Kα intensity can be observed until the beam reaches

position 3. In reality, the model of Fig.13b is probably too simplistic in the sense that the edge between the Na and K-rich phases may not be a straight line or perpendicular to the surface of the mineral.

5. SRXRF at third generation synchrotron sources.

A number of the above discussed limitations of SRXRF can be eliminated by using more intense photon sources. At currently operation storage rings, this can be done by using undulator or wiggler radiation instead of X-rays originating from a bending magnet. Rivers et al. have discussed SRXRF experiments at the 5T superconducting wiggler of NSLS beamline X17B1. Next to the advantage brought by the higher intensity of the source, they point out that as a result of the higher divergence of the wiggler beam in the vertical plane, a poorer degree of polarisation of the microbeam is obtained that at the X26A bending magnet beamline.
An alternative is to employ bending magnet radiation from one of the third generation synchrotron rings now currently under construction in the Japan (SPRing-8 in Harima), the US (APS at Argonne National Laboratories, Illinois) and in Europe (ESRF in Grenoble, France). For the latter facility, whose construction phase is drawing to a close, we have estimated the expected improvement in flux density and achievable MDL's when a collimated X-ray microprobe would be installed at a 0.8 T bending magnet beam line. The predictions are based on a detailed Monte Carlo simulation of the interaction of a polarised, polychromatic photon beam with sample atoms (Vincze et al., 1992a; Janssens et al, 1992). The details of these calculations, which also include a comparison of the performance of optical devices for generating

high energy X-ray microbeams other then pin holes, are presented elsewhere (Vincze et al., 1992b).

In general, however, compared to the SRXRF spectrometer at the NSLS X26A beamline, an increase in flux density by a factor of 50 is obtained. As the critical energy of the ESRF (19.6 keV) is much higher than that of the NSLS (5.9 keV), the ESRF spectrometer is also expected to be more sensitive for determination of heavier elements than the NSLS instrument (Van Langevelde et al., 1992). The 50-fold increase in fluxdensity also implies that at the ESRF, approximately the same flux will be concentrated into a 2x2 μm^2 area as is currently available in an 8x8 μm^2 spot at the NSLS.

In terms of the above discussed applications, this means that it will be possible to analyse particles with sizes down to 1-2 μm diameter or alternatively to characterise 50 times more particulates in the size range 5-20 μm in the same time are currently required at the NSLS. With respect to trace element imaging applications, e.g., for the investigation of biological materials, a 2x2 μm^2 beam will allow the visualisation of the distribution of chemical elements in single (living) cells. If large beam sizes are employed, a substantial reduction in acquisition time can be expected. E.g., the time necessary to acquire the X-ray maps of Fig. 10 would reduce from 12h to ca. 15 min., making the X-ray microprobe a much more interactive type of analytical technique than currently is the case.

6. Conclusions.

In this work, a comparison was made between SRXRF and more conventional microanalytical techniques such as EPXMA and SIMS. The applicability of SRXRF to two typical microanalytical problems, namely the characterisation of individual particles and the mapping of trace elements in solids was evaluated. It was concluded that SRXRF is a valuable method for analysis of trace, minor and major elements and that it could be used profitably in parallel with electron- and ion-beam methods.

With respect to analysis of microscopic particles, one can conclude that using EPXMA and white light SRXRF, the same major particle classes can be identified, even when only a limited number of particles are analysed, Whereas by means of SRXRF, information on the trace constituents can readily be obtained, the applicability of the method is limited by the long counting times which are needed to extract this information from each particle and by the fact that only coarse mode aerosols can be analysed. These limitations, however can be overcome by using more brilliant X-ray sources. Another limitation is the very low sensitivy of current SRXRF instruments for low Z elements.

A complementary scheme of particle characterisation in which the two methods are used appears most promising. In such a scheme, first automated EPXMA could be used to identify and determine the abundance and major composition of the various groups in the aerosol population; in a second phase, SRXRF could be employed to

obtain (more accurate) information on the major and trace level composition of some or all the particle classes by analysing a limited number of aerosols.

The applicability of SRXRF for accurate mapping of trace elements with atomic number > 20 in a non-destructive is evident. However, current analytical procedures which can reliably convert X-ray images collected from heterogeneous, non-thin samples into concentration maps still lack sophistication. Quantitative analysis of the image data in this type of samples is primarily hampered by the high penetration of the primary photon beam, which in this type of samples also limits the lateral resolution of SRXRF to 10-20 μm in the 45°/45° measuring geometry. In this respect, the evaluation of the (dis)advantages of using other geometries (such as 5°/85° or 0°/70°), which do not yield optimal sensitivity/MDL's but a higher lateral resolution, may be of interest. Similarly the combination of two-dimensional mapping with differential absorption and/or fluorescent microtomography may provide a solution to these quantification problems. The problem obviously vanishes if sufficiently thin specimen are employed.

Predictions of the performance of a white light SRXRF spectrometer installed at a bending magnet of a third generation storage ring indicated improvements in flux density by a factor of 50, elimitating some of the above-mentioned limitations of present day SRXRF instruments.

Acklowledgements.

K.J. is a fellow of the Belgian National Science Fund, Brussels, Belgium; this work is sponsored by FKFO (Brussels) Grant Nr. 2009291N. The authors are indebted to W. Dorrine and W. Saenen for assisting with the EPMA word and to J. Van Vooren and W. Van Hoolst for the SIMS measurements. This research was also supported by the US Department of Energy, Office of Basic Energy Sciences, Chemical Sciences Division under Contract No. DE-AC02-76CH00016. M.R. wishes to thank the National Science Foundation (N.S.F.) for support through grant No. EAR89-14669.

References.

Artaxo P., Andrade F., Maenhaut W., Trace Elements and Receptor Modelling of Aerosols in the Antarctic Peninsula, Nucl. Instr. Meth., B49 (1990) 383-387.

Bavdas M., Knöchel A., Ketelsen P., Pertersen W., Gurker N., Salehi M.H., Dietrich T., Imaging Multielement Analysis with Synchrotron Radiation Excited X-ray Fluorescence Radiation, Nucl. Instr. Meth. A266 (1988) 308.

Baryshev V.B., Kulipanov G.N., Zavtsev E.I., Terekhov Y.V., Kalyuzny V.I., Sensitive X-ray Fluorescence Analysis of Geological Samples using Synchrotron Radiation, Nucl. Instr. Meth., A261 (1987) 279.

Bernard P., Van Grieken R., Eisma D., Classification of estuarine particles by automated electron microprobe analysis and multivariate cluster techniques, Envir. Sci. Technol., 20 (1986) 467-473.

Bodhaine B.A., Deluisi J.J., Harris J.M., Houmere P, Bauman S, Pixe Analysis of South Pole Aerosol, Nucl. Instr. Meth., B22 (1987) 241-247.

Bos A.J.J., Vis R.D., Verheul H., Prins R., Davies S.T., Bowen D.K., Makjanic J., Valkovic V., Experimental Comparison of Synchrotron Radiation with other modes of Excitation of X-rays for Trace Element Analysis, Nucl. Instr. Meth., B3 (1984) 232.

Frantz J.D., Mao H.K., Zhang Y., Wu, Y, Thompson A., Underwood J., Giauque R., Jones K., Rivers M, Analysis of fluid inclusions by X-ray Fluorescence using Synchrotron Radiation, Chemical Geology, 69 (1988) 235-244.

Gocssens D. Van't Dack L., Gijbels R., Ion-microprobe analysis of rock-forming minerals from the Carnmenellis Granite, in: Water-Rock Interaction, D.L. Miles, Edr., Balkema, Rotterdam/Brookfield, 1989, p. 267-270.

Goshi Y., Aoki S., Iida A., Haykawa S., Yamaji H., Sakurai K., Jpn. J. Appl. Phys., 26 (1987) L1260.

Kwiatek W.M., Long G.J., Reuhl K.R., Hanson A.L., Jones K.W., Pounds J.G., Toxicologist, 7(1) (1987) 302a.

Janssens K., Van Borm W., Van Espen P., Increased Accuracy in the Automated Interpretation of Large EPMA Data Sets by the Use of an Expert System, NBS J. of Research, 93(1) (1988) 260-264.

Janssens K., Van Langevelde F., Adams F.C., Vis R.D., Sutton S.R., Rivers M.L., Jones K.W., Bowen D.K., Comparison of Synchrotron X-ray Microanalysis with Electron and Proton Microscopy for Individual Particle Analysis, Adv. X-ray Anal., 38 (1992) 215.

Janssens K., Vincze L., Van Espen P., Adams F., Monte Carlo simulation of conventional and synchrotron energy-dispersive X-ray spectrometers, X-ray Spectrom., 1992, submitted.

Jones K.W., B.M. Gordon, A.L. Hanson, J.B. Hastings, M.R. Howells, H.W. Kraner, J.R. Chen, Applications of Synchrotron Radiation to Elemental Analysis, Nucl. Instr. Meth., B3 (1984) 225.

Jones K.W., Gordon B.M., Trace Element Determinations with Synchrotron-Induced X-ray Emission, Anal. Chem., 61 (1989) 341A.

Jones K.W., Spanne P, Schidlovsky G., Xue D., Bockman R., Rabinowits M., Hammond P., Bornschein R., Hoeltzel D., Calcified-Tissue Investigations Using Synchrotron X-ray Microscopy, in: X-ray Microscopy III, A. Michette, G. Morrison, C. Buckley, Eds., Springer Verlag Berlin, 1992, p. 431.

Mazzolini A.P., Legge G.J.F., Palaghy C.K., The distribution of Trace Elements in Mature Wheat Seed using the Melbourne Proton Microprobe, Nucl. Instr. Meth., 191(1981) 217.

Raeymaekers B., Characterisation of particles by automated electron probe microanalysis, PhD. Thesis, University of Antwerp, 1986.

Spanne P., Rivers M.L., Computerized Microtomography using Synchrotron Radiation from the NSLS, Nucl. Instr. Meth., B24/25 (1987) 1063.

Sparks C.S., in Synchrotron Radiation Research, H. Winick, S. Doniach, Eds., Plenum Press, New York, 1980, Chapter 14.

Thompson A.C, Underwood J.H., Wu Y., Giauque R.D., Jones K.W., Rivers M.L., Elemental measurements with an X-ray microprobe of Biological and Geological samples with Femtogram sensitivity, Nucl. Instr. Meth., A266 (1988) 318.

Torok Sz., Szökefaldvi-Nagy Z., Sándor S., Baryshev V.B., Zolotarev K.V., Kulipanov G.N., Comparison of X-ray Emission Analysis Sensitivity under various techniques of excitation in Biological and Environmental Studies, Nucl. Instr. Meth., A282 (1989) 499.

Van Langevelde F., Bowen D.K., Tros G.H.J., Vis R.D., Huizing A., de Boer DKG, Ellipsoid X-ray Focussing for Synchrotron Radiation Microprobe Analysis at the SRS, Daresbury, UK, Nucl. Instr. Meth., A292 (1990) 719.

Vincze L., Janssens K., Adams F., A general Monte-Carlo simulation of ED-XRF spectrometers, Part I: Unpolarised radiation, homogeneous samples, Spectrochimica Acta B, submitted, 1992.

Vincze L., Janssens K, Adams F., Riekel C., Micro-focus X-ray optics for Synchrotron Radiation induced X-ray Fluorescence at the ESRF, Proc. 12th Int. Conf on X-ray Optics and Micro Analysis, Manchester, September 1992.

Vis R.D., Scanning Microscopy, 2 (1988) 977.

Table I. Characteristics of various microanalytical techniques. (adapted from K. Traxel, Nucl. Instr. Meth., A268 (1988) 567-578)

	Projec-tile	Quantum Energy (keV)	Destructive ?	Spot size (μm)	Penetration depth (μm)	MDL (ppm)	Accuracy
SIMS	M^+, N^-	10-30	yes	< 1	0.010	< 1	w.t. 10%
LAMMA	hν		yes	~ 1	1	~ 1	w.t. 50%
μ-PIXE	p^+, α	2-3 10^3	y/n	0.3	5-100	5-10	b.t. 10%
EPMA	e^-	5-100	no	< 0.1	1-5	> 100	b.t. 20%
XRM	X	10-50	no	3-15	10-1000	1-100	b.t. 5%

SIMS = Secondary Ion Microscopy; LAMMA = Laser Microprobe Mass Analysis
PIXE = Particle Induced X-ray Emission, EPMA = Electron Probe Micro Analysis
b.t. = better than; w.t. = worse than

Table II. Average bulk composition of albite and K-feldspar phase in microcline perthite.

	K-feldspar matrix	exsolution lamellae
	Matrix (EPMA) (%)	
Na_2O	0.6 %	11
Al_2O_3	18.9 %	20.1
SiO_2	64.7 %	68.
K_2O	16.6 %	0.22
CaO		0.17
	Traces (SIMS) (ppm)	
Li_2O	13	0.9
Rb_2O	840	3.0
SrO	480	9.5
Cs_2O	7.9	0.14
BaO	48	3.2

Adapted from D. Goossens et al., 1989.

Table III. Characteristics of the various particles classes found by hierarchical clustering of elemental electron and photon induced X-ray intensities of the Antarctican Aerosol particles.

	EPXMA		SRXRF	
	group abundance (%)	group composition (% X-ray intensity)	group abundance (%)	group composition (% X-ray intensity)
SUMMER	41	Cl(95),Na(5)	51	Cl(70),S(1),Br(1)
	28	Cl(34),S(29),Mg(28),K(23)	14	Cl(28),Ca(20),S(2)
	14	Cl(71),S(15),Mg(11)		
	10	Ca(46),S(47)	10	Ca(54),S(2),Sr(1)
	4	Si(37),Cl(23),Fe(11), Al(8),Mg(7),S(5),K(4)	7	Fe(70)
	3	Si(56),Al(22),K(12),Cl(6)		
WINTER	55	Cl(92),Na(6),S(1),Ca(1)	45	Cl(80),K(3),Ca(3),Br(2)
	25	Cl(87),Na(5),K(1),Ca(1)		
	7	Cl(76),S(10),K(5),Na(4),Ca(3)		
	5	Cl(57),S(17),Mg(9)		
	5	S(36),Cl(25),K(20),Mg(8),Ca(8)	37	Cl(54),K(4),Ca(20),S(3), Br(3),Sr(1),Cu(.5),Zn(.5)
	3	Cl(75),Mg(22),S(2)	18	Br(25),Cl(13),K(12), Ca(11),Zn(10),S(1),Ni(1)

Table IV. Concentrations of selected minor and trace constituents of NaCl microcrystals (see text for details). Values are expressed in ppm, unless otherwise indicated.

	S (%)	K	Ca	Fe	Zn	Br	Sr	Pb
1	0.43	65	300	14	5	41	8	9
2	0.39	112	54	17	2	87	39	26
3	0.41	-	14	7	2	21	2	24
4	0.45	54	10	19	2	109	7	15
5	0.40	32	14	87	1	50	-	6
6	0.42	-	71	19	2	34	13	11
7	0.46	55	280	32	5	114	5	65
8	0.44	-	67	17	1	45	3	27
9	0.46	-	125	5	6	32	5	150
10	0.42	96	38	14	4	54	-	26
Average	0.43	41	97	23	3	59	8	36
Std. Dev.	0.02	41	106	24	2	33	11	43

Table VI. Calculated maximum Fe concentration in the Fe-rich inclusion shown in Fig. 11 as a function of the assumed depth of the inclusion in the mineral (see text for details).

Equivalent Inclusion Depth d (μm)	Maximum Fe Concentration c_{Fe} (μg/cm²)	Absorption Factor A_{Fe} (see Eq.2)
0	3.9 ± 0.1	1.0
10	5.5 ± 0.1	0.7
20	7.7 ± 0.2	0.5
30	11.1 ± 0.3	0.35
40	15.4 ± 0.4	0.24

Figure Captions.

Figure 1. *Quantum efficiency of photon, electron and proton induced X-ray emission.*

Figure 2. NaCl microcrystals on a Nuclepore filter sampled in the Antarctic. The diameter of the pores is 8 μm.

Figure 3. Backscattered electron image of microcline perthite. Horizontal field width is 300 μm. Albite exsolution (dark) lamellae in a K-feldspar matrix (light) are visible. Dimensions of large lamella parallel and perpendicular to black line are approx. 140 x 30 μm.

Figure 4. Energy dispersive X-ray spectra of the NaCl microcrystals shown in Fig. 2. (a) Electron induced X-ray spectrum, showing characteristic peaks of matrix elements, (b) synchrotron radiation induced XRF spectrum, showing trace element lines.

Figure 5. X-ray spectra of soil dust particles cbtained by means of (a) EPXMA, (b) SRXRF.

Figure 6. Cluster diagrams of X-ray data derived from the Antarctican winter aerosols using (a) SRXRF, (b) EPXMA.

Figure 7. Loading plot of trace elements on the first two principal components derived from X-ray data on the Cl-rich aerosols found in the summer sample.

Figure 8. Electron induced X-ray maps of the large exsolution lamella shown in Fig. 3. (a) Na-Kα, (b) K-Kα.

Figure 9. Secondary ion images of major and trace elements obtained from the same area as shown in Fig. 8. Left to right, top to bottom: ^{7}Li, ^{11}B, ^{23}Na, ^{27}Al, ^{30}Si, ^{39}K, ^{40}Ca, ^{55}Mn, ^{56}Fe, ^{85}Rb, ^{89}Y, ^{90}Zr, ^{93}Nb, ^{98}Mo, ^{138}Ba and ^{208}Pb.

Figure 10. Synchrotron radiation induced X-ray maps of the area shown in Fig. 8. Left to right, top to bottom: K-Kα, Ca-Kα, Ti-Kα, Mn-Kα, Fe-Kα, Pb-Lα, Rb-Kα, Sr-Kα.

Figure 11. Electron and photon induced X-ray spectra of the albite and K-feldspar phase of the microcline perthite. Albite phase: (a) EPXMA spectrum, (b) SRXRF spectrum; K-feldspar phase: (c) EPXMA spectrum, (d) SRXRF spectrum.

Figure 12. Surface plot of the Fe-Kα intensity near the location of the Fe-rich inclusion.

Figure 13. (a) Cross sections of the K-Kα X-ray and ^{39}K ion images along the black line shown in Fig. 3. (b) In-depth model of the structure of the albite lamella; the position of the photon beam at various locations, before, at and after the edge is also shown.

Fy 1

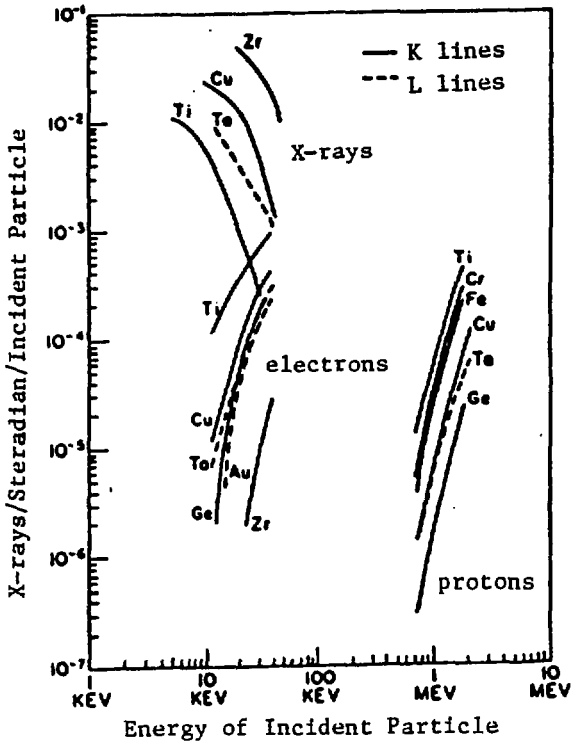
K lines
L lines
X-rays
electrons
protons
Zr
Cu
Ti
Te
Ti
Cu
Ta
Au
Ge
Zr
Ti
Cr
Fe
Cu
Te
Ge
X-rays/Steradian/Incident Particle
Energy of Incident Particle
1 KEV
10 KEV
100 KEV
1 MEV
10 MEV

Fig 2 ... quality of original picture ... (letter)

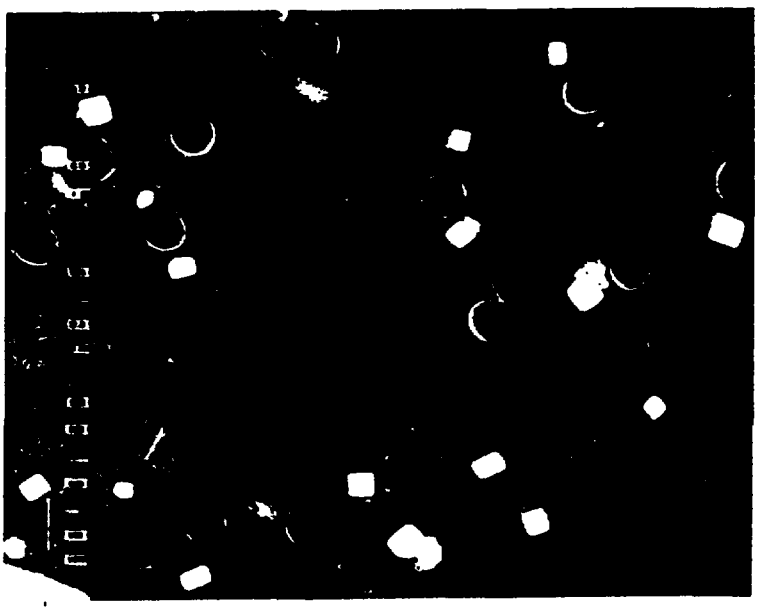

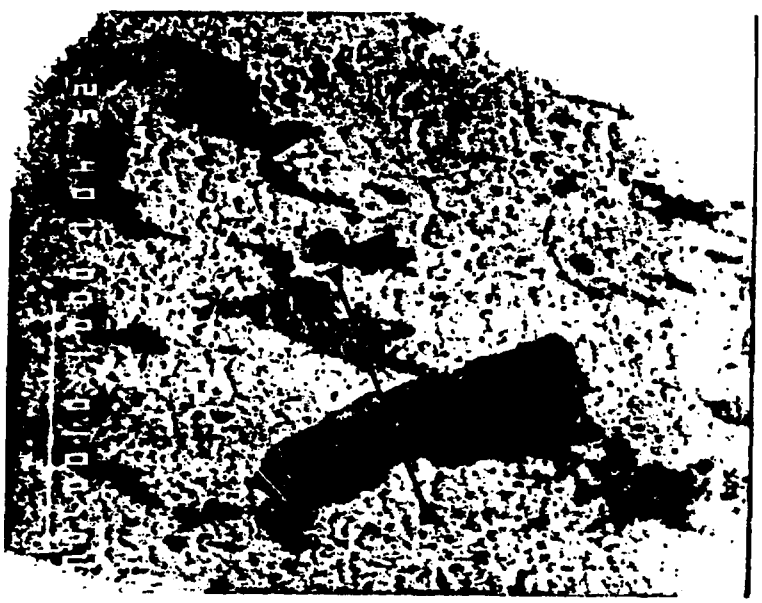

Fig 4

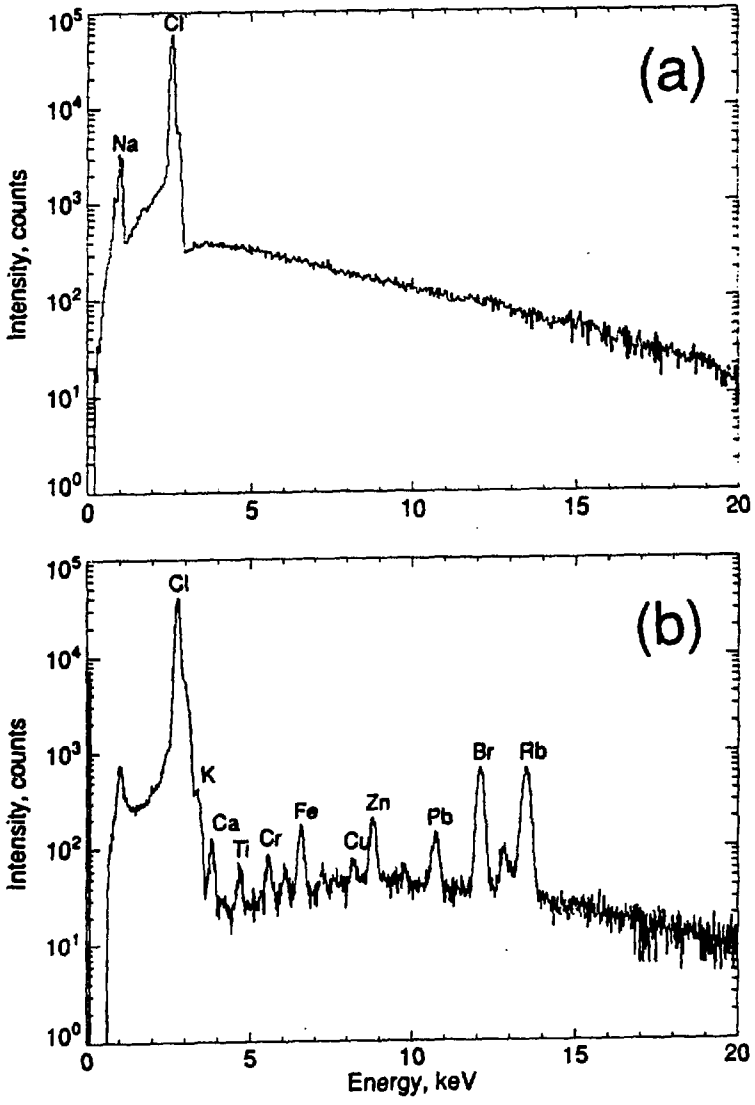
(a)
Cl
Na
Intensity, counts
10^5
10^4
10^3
10^2
10^1
10^0
0
5
10
15
20
(b)
Cl
K
Ca
Ti
Cr
Fe
Cu
Zn
Pb
Br
Rb
Intensity, counts
Energy, keV

Fig 5

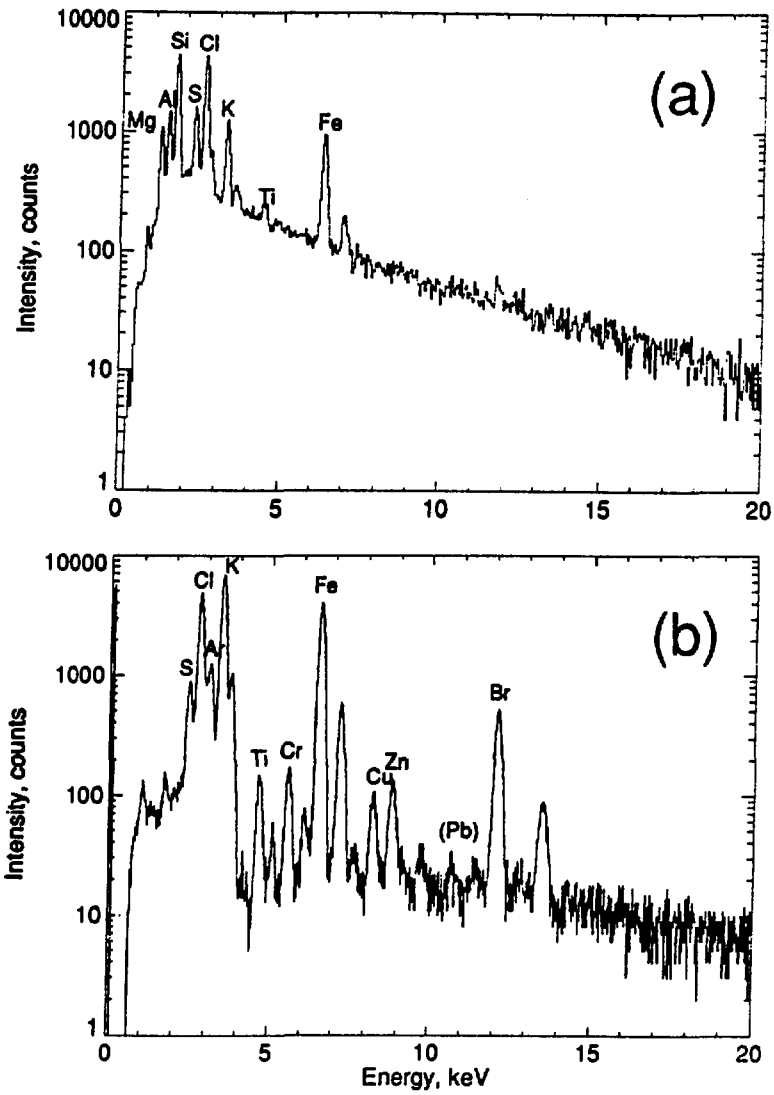
(a)
Intensity, counts
10000
1000
100
10
1
Mg
Al
Si
S
Cl
K
Ti
Fe
0
5
10
15
20
(b)
Intensity, counts
10000
1000
100
10
1
S
Ar
Cl
K
Ti
Cr
Fe
Cu
Zn
(Pb)
Br
0
5
10
15
20
Energy, keV

(a)

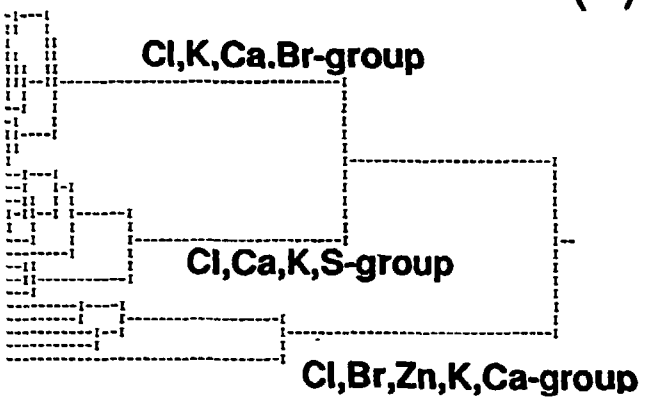
Cl,K,Ca.Br-group
Cl,Ca,K,S-group
Cl,Br,Zn,K,Ca-group

(b)

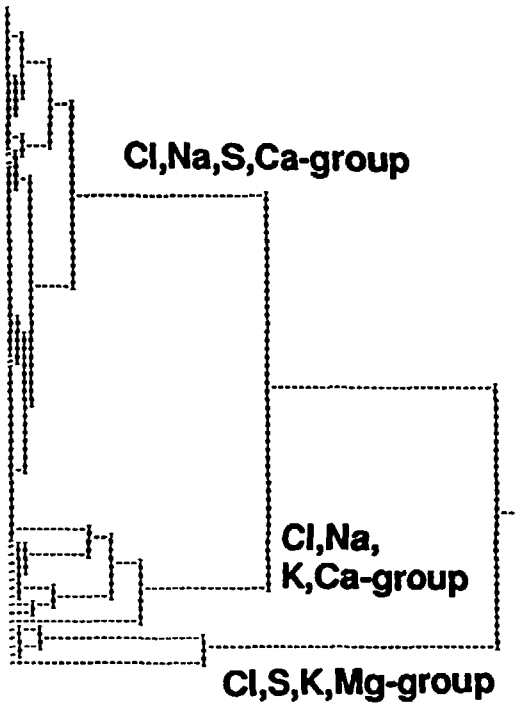
Cl,Na,S,Ca-group
Cl,Na,
K,Ca-group
Cl,S,K,Mg-group

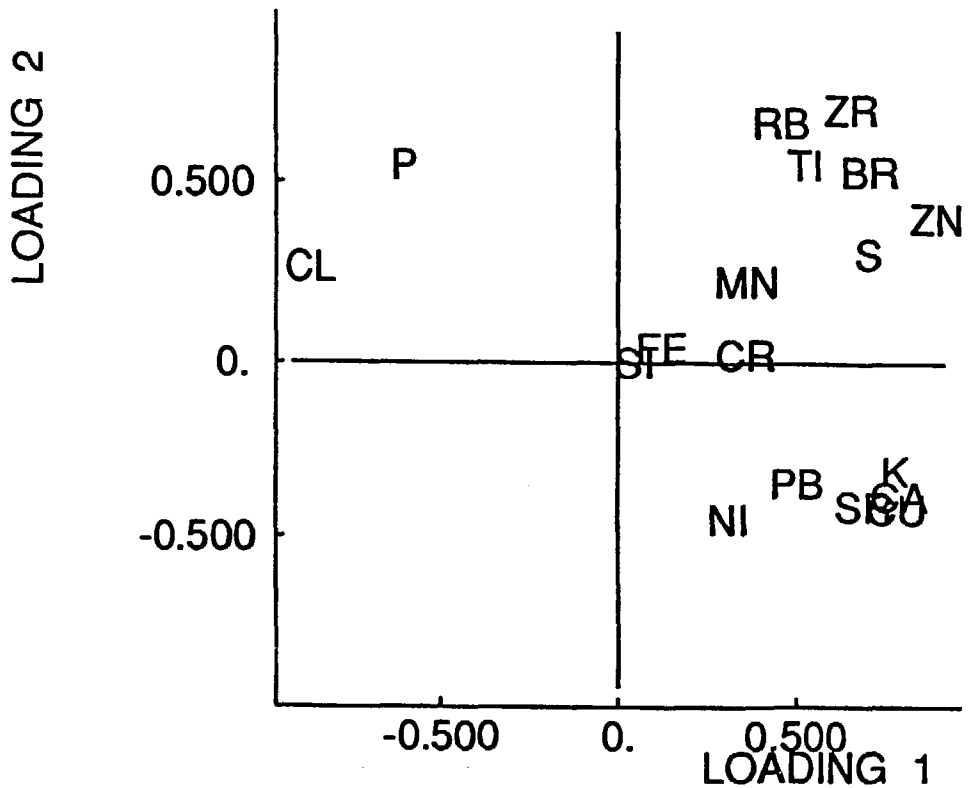
LOADING 2
0.500
0.
-0.500
P
CL
RB
ZR
TI
BR
ZN
S
MN
FE
CR
SI
K
PB
NI
-0.500
0.
0.500
LOADING 1

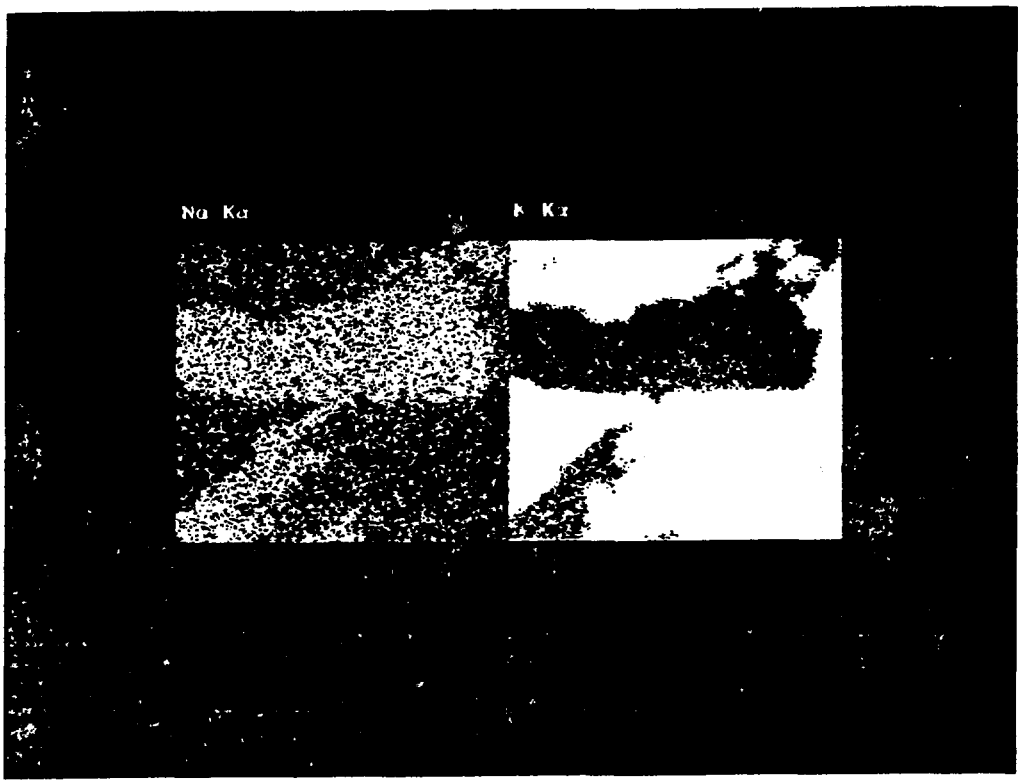
Na Kα
K Kα

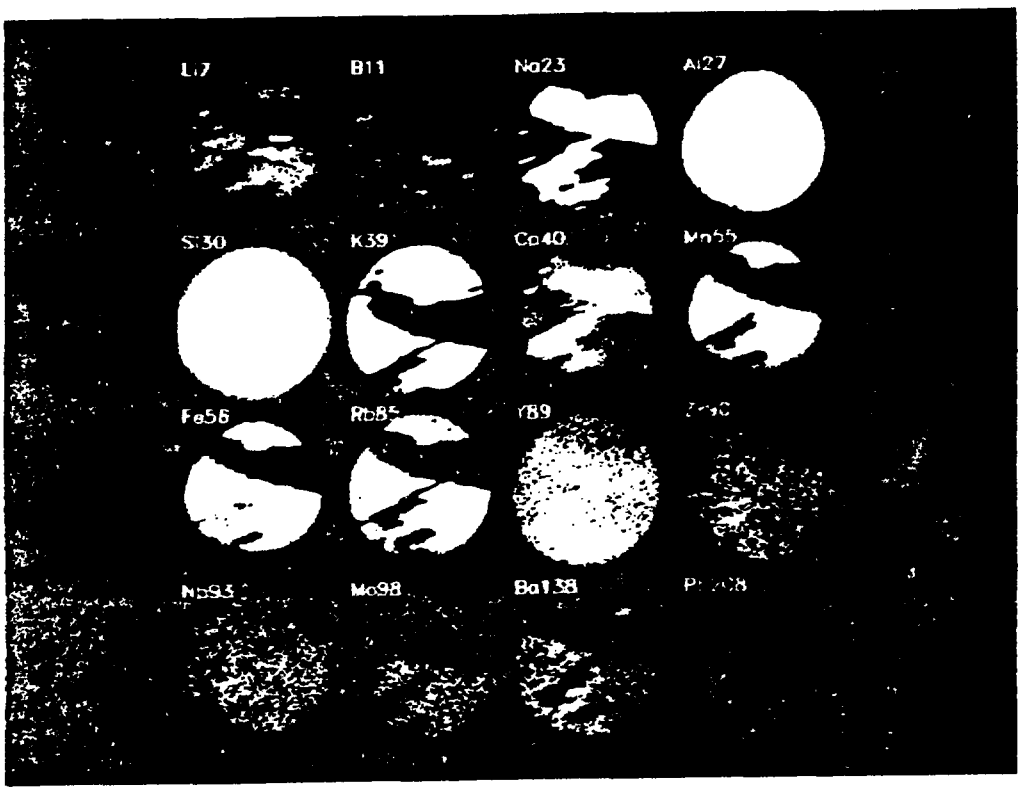
Li7
B11
Na23
Al27
Si30
K39
Co40
Mn55
Fe56
Rb85
Y89
Nb93
Mo98
Ba138

Fe-Kα
Ka

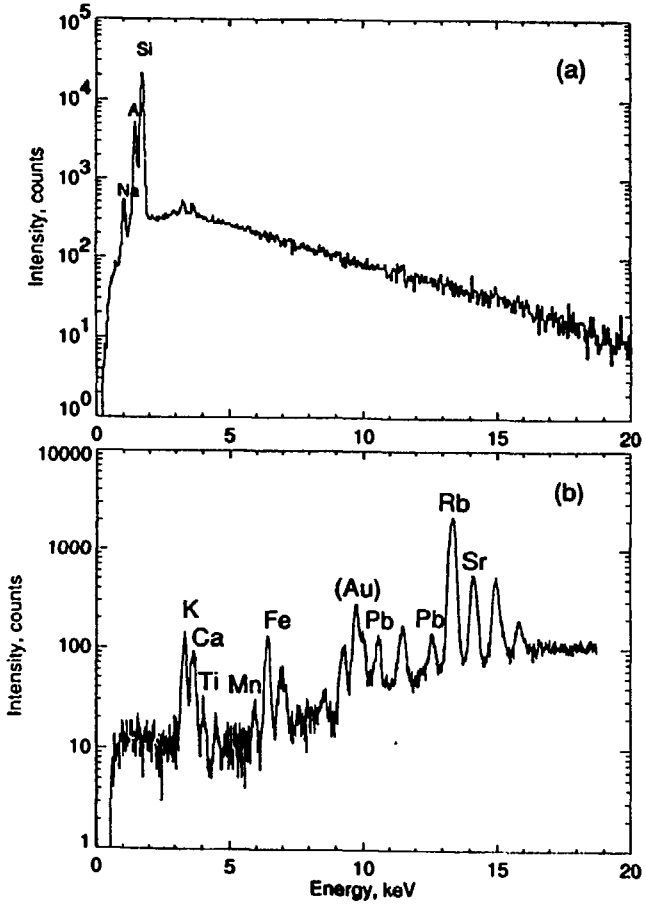
(a)
Si
Al
Na
Intensity, counts
(b)
K
Ca
Ti
Mn
Fe
(Au)
Pb
Pb
Rb
Sr
Intensity, counts
Energy, keV

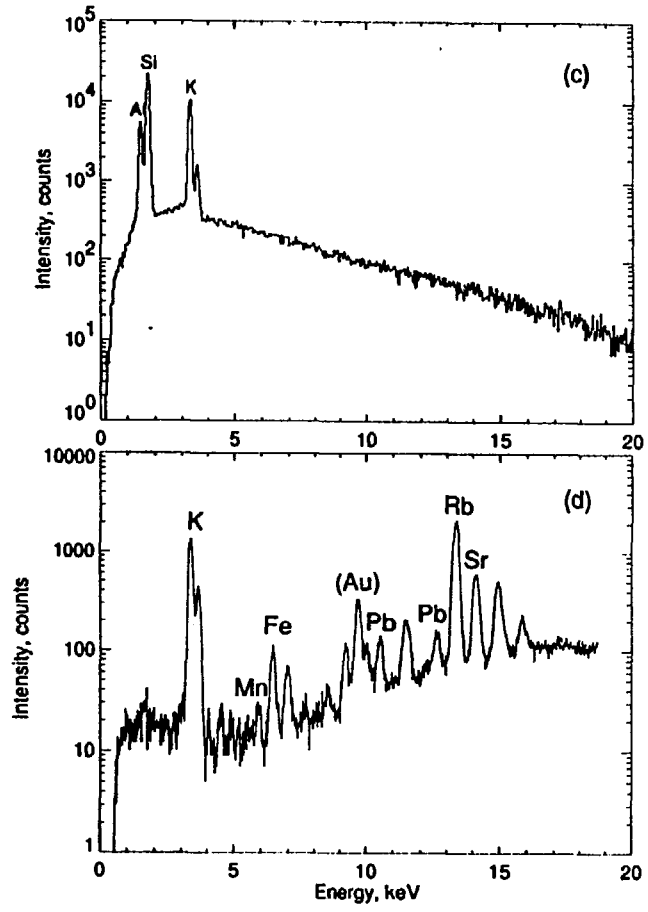
(c)
Si
Al
K
Intensity, counts
(d)
K
Mn
Fe
(Au)
Pb
Pb
Rb
Sr
Intensity, counts
Energy, keV

F. 12

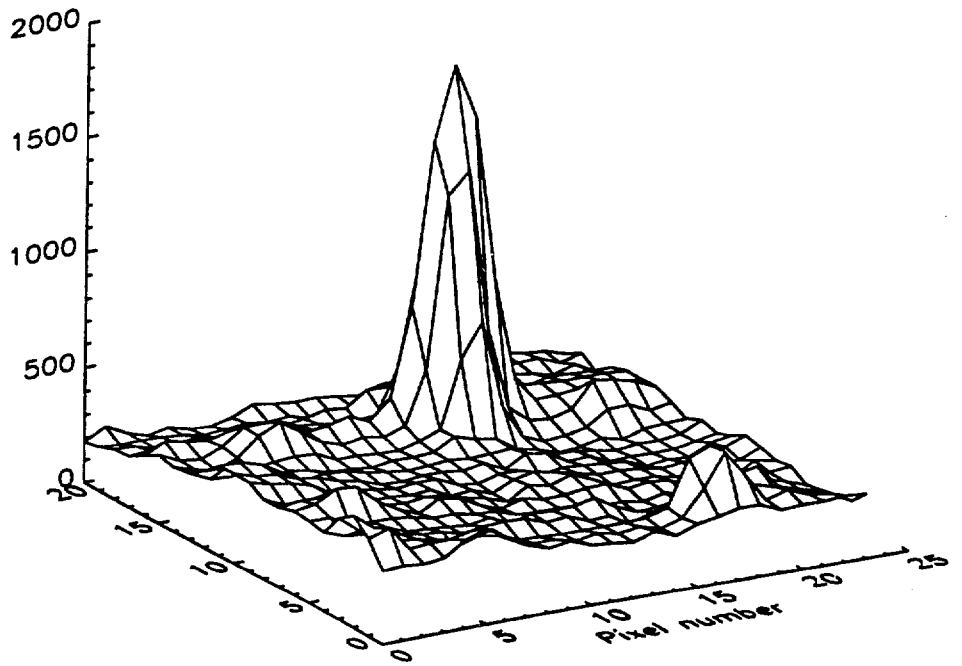

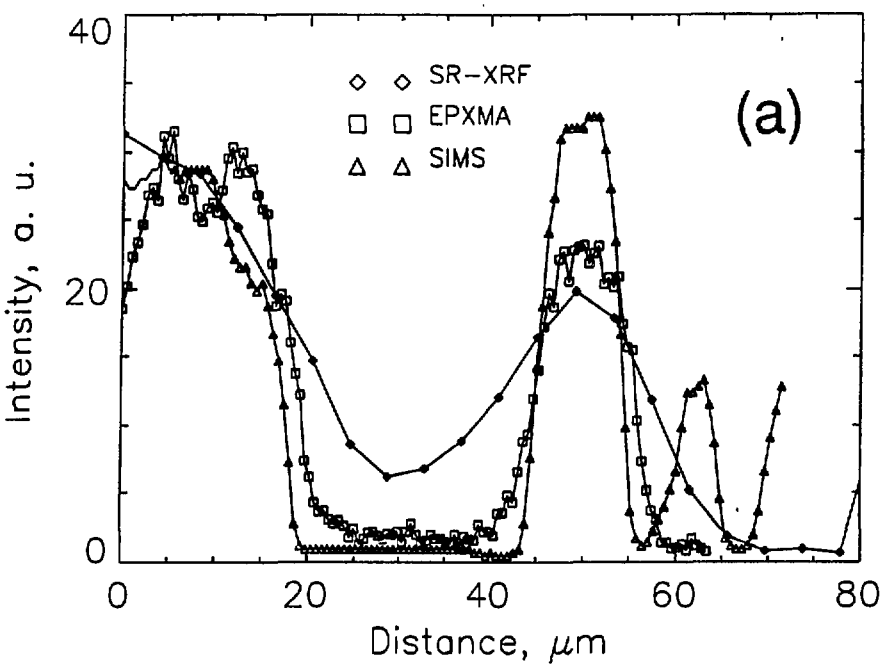
40
20
0
Intensity, a. u.
SR-XRF
EPXMA
SIMS
(a)
0
20
40
60
80
Distance, μm

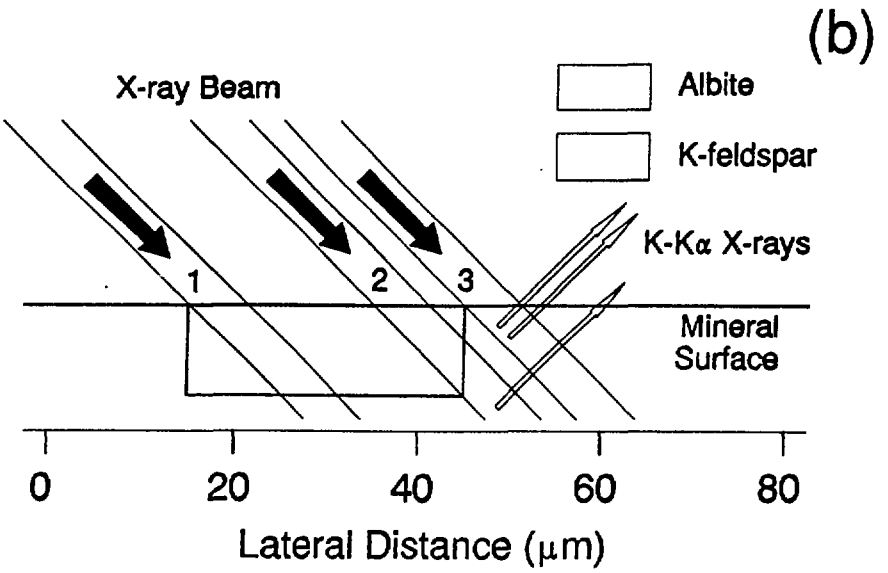
(b)
X-ray Beam
Albite
K-feldspar
K-Kα X-rays
1
2
3
Mineral
Surface
0
20
40
60
80
Lateral Distance (μm)